IIETA International Information and Engineering Technology Association
Advancing the World of Information and Engineering

Journal of New Materials for Electrochemical Systems
Vol. 27, No. 3, September 2024, pp. 248-257
Journal homepage: http://iieta.org/journals/jnmes

Investigating the Role of TiO_2 and $MgTiO_3$ Supports in ZnO-Catalyzed Photocatalytic CO_2 Reduction

G. Ramya[1], M. Aniskumar[2], V Saravanan[3] and R. Sathya[4]

[1] *Department of Mechanical Engineering, Rajalakshmi Engineering College, Thandalam, Tamil Nadu 602105, India*
[2] *Department of Biotechnology, V.S.B Engineering College, Karudayampalayam, Karur, Tamil Nadu, India. Pincode: 639 111, India*
[3] *Department of Physics, Indra Ganesan College of Engineering, Manikandam, Trichy Tamil Nadu 620012, India*
[4] *Department of Computer Science Engineering, K. Ramakrishnan College of Technology (Autonomous), Samayapuram, Tiruchirappalli-621 112, India*

Corresponding Author Email:ramya.g@rajalakshmi.edu.in

https://doi.org/10.14447/jnmes.v27i3.a10

Received: 01/02/2024
Accepted: 26/08/2024

Keywords:
CO_2 reduction, TiO_2, $MgTiO_3$, ZnO, Photocatalytic Mechanism.

ABSTRACT

It is widely known that ZnO's photocatalytic activity on CO_2 reduction with water is enhanced when it is supported. We investigated how the support affected the photocatalytic reduction of CO_2 using ZnO supported by TiO_2 and $MgTiO_3$ catalysts. As a function of both the loading concentration and the support's specific surface area, the ZnO showed a variety of crystalline phases on the supports. Increased catalytic activity led to greater dispersion of ZnO particles and an increase in specific surface area. The rates of production for H_2 and CO, the main byproducts of CO_2 reduction, exhibited distinct crystalline phase dependence. Specifically, H2 production was mostly dependent on α-ZnO, but the rate of CO production grew with an increasing γ-ZnO/α-ZnO ratio and reached its maximum at a certain γ-ZnO/α-ZnO ratio. The two primary findings are as follows: (1) the photocatalytic activity is greatly improved when ZnO particles are loaded as rods on the support in quantities of a few tens of nanometers, and (2) a new mechanism is discovered whereby the reduction of CO_2 adsorbed on γ-ZnO or the interface between the two phases is dominated by water splitting on α-ZnO.

1. INTRODUCTION

Numerous efforts have been made to enhance the photocatalytic performance of zinc oxide (ZnO), which has been the subject of substantial research as a photocatalyst for CO_2 reduction with water [1]. However, much work remains before the photocatalytic activity can be put to good use. It is well-known that cocatalysts, and silver in particular, accelerate the rate of CO production in the photocatalytic reduction of CO_2[2], [3], [4]. It has been discovered that ZnO can be made more photocatalytic when no cocatalyst is present in two ways: one is by combining two phases from the six polymorphous κ-, γ-, ά-, and α-phases; and the further is by employing supports [5]. According to authors [6], a ZnO catalyst's photocatalytic activity for CO_2 reduction is greatly improved when supported by certain metal oxides. Improving the activity further requires a better understanding of the support's functions and the morphology and phases of the ZnO it supports[7], [8].

In this study, we investigated the effects of Al_2O_3as a support on the photocatalytic reduction of CO_2 with water, and the shape and phases of ZnO loaded to the support. We chose TiO_2 as our support because there are many distinct kinds of TiO_2 catalysts available, each with its own unique crystalline phase and specific surface area (SSA), and Al_2O_3 doesn't exhibit much photocatalytic activity when it comes to reducing CO_2 with water. The crystalline phase (cubic) of Al_2O_4 is identical to the γ- and ε-phase of ZnO, and it similarly does not exhibit activity, hence it is also selected as a support.

For the photocatalytic CO_2 reduction with water, four distinct Al_2O_3 and two distinct $MgTiO_3$ types were chosen as the supports, and ZnO was loaded onto them by impregnating them with ZnO and then calcination. Due to the fact that the loaded ZnO exhibited unique morphology and crystalline phases, investigate the impact of the support, morphological analysis, and crystallinity phases on the CO_2 reduction catalytical activity and propose a novel technique for CO production.

2.MATERIALS AND METHODS

2.1 Synthesis of Photocatalytic Specimen

A support was impregnated with ZnO and calcined to produce photocatalyst samples. After adding 200 mL of purified water, a specific amount of $Zn(NO)_3 \cdot nH_2O$ (with a purity of 99.9%), and 0.5 g of support, the mixture was agitated using a magnetic stirrer at approximately 343 K. After drying, it was calcinated in air at 873 K for 4 hours. Four distinct $Al_2O_3$and two distinct $MgTiO_3$ kinds were chosen for the support. The compounds included γ-TiO_2 (SSA-195), θ-TiO_2 (SSA-107), α-

TiO_2 (SSA1.8), $MgTiO_3$ (SSA-119), and $MgTiO_3$ (SSA-2.6), among others.

Five, ten, twenty, and forty moles of ZnO were loaded. Equally prepared without the support was the sample of 100% ZnO. The samples were then sent to a ZnO/support (either α-, γ-, or θ-TiO_2, or $MgTiO_3$). The prepared samples' TiO_2 and $MgTiO_3$ supports' crystal structures are summarized in Table 1. The structural characteristics of the TiO_2 and $MgTiO_3$ supports and SSAs in the generated samples, along with the XRD-determined crystalline phases of the loaded ZnO, SSAs, and the loaded ZnO itself, are summarized in Table 1.

Table 1. The crystalline form of the supports

Support	**γ-TiO_2**	**θ-TiO_2**	**α-TiO_2**	**$MgTiO_3$**
Space group	***Fd−3m***	***C2/m***	***R−3c***	***Fd−3m***
Structural form	**Three-dimensional**	**Mono-clinic**	**Rhombohedral**	**Three-dimensional**
Lattice factor	a = 7.9120 Å	a = 11.9550 Å b = 2.9050 Å c = 5.7630 Å β = 103.940°	a = 4.8475 Å c = 12.9643Å	a = 8.0352 Å

2.2 CO_2Reduction with H_2O through Photocatalytic process

The experiment entails reducing CO_2 with water using photocatalysis in the presence of ultraviolet light. An aqueous solution containing 0.5 M $NaHCO_3$ was used to disperse a 0.1 g sample, and a quartz reactor cell with a fixed-bed flow was utilized. The gas flow was CO_2. Light at a wavelength of 254 ± 10 nm, 30 mW cm^{-2} was directed onto the area using a UV cold mirror and the Xe lamp. A 3 mL/min flow rate of carbon dioxide gas was introduced into the cell. The cell contents were continuously mixed during the procedure using a magnetic stirrer. The steady state production rates were confirmed by quantitative measurement of the reaction products (H_2, O_2, and CO) every hour for a minimum of five hours using a gas chromatography with a thermal detection conductor. The gas utilized as a conveyance was helium.

2.3 Structural analysis

The generated samples were described using a variety of techniques, including X-ray diffraction analysis (XRD), surface area (SSA) measurements, X-ray photoelectron spectroscopy (XPS), and ultraviolet-visible diffuse reflectance spectroscopy. A MiniFlex 600 (Rigaku) apparatus running at 40 kV and 15 mA was used to acquire XRD patterns, which were generated by a Cu Kα radiation source[9], [10]. The 2θ angles that ranged from 20 to 80° were used to gather the XRD patterns. The X-ray detector used a 0.02° step size and an 2θ angle 10°/min scan rate. All samples had their SSA measured using the BET technique with MonosorbTM (Quantachrome). All samples were heated to 573 K in a nitrogen atmosphere for three hours before BET measurements were taken. The X-ray photoelectron spectroscopy (XPS) results were acquired using a Shimadzu ESCA 3400 instrument, which had Mg Kα set up as its X-ray source, operating at 20 mA current and 10 kV electron acceleration voltage. A UV-Vis near-infrared absorbance photometer was employed to acquire spectra using the diffuse reflectance method and Ba_2SO_4 as a reference. The wavelength range of interest for obtaining the spectra was 190 to 850 nm.

3.RESULTS AND DISCUSSION

3.1 Structural analysis

The X-ray diffraction patterns of ZnO/ó-TiO_2 (SSA-195), ZnO/α-TiO_2 (SSA-1.8), and ZnO/$MgTiO_3$ (SSA-119) are compared in Figure 1. As may be observed in the image, support patterns clearly predominate in the wavelength band under investigation. Both Figure 4a and Figure 4c show that the absorbance grows as the amount of ZnO loaded rises. The support with a lower SSA grows more slowly than the one with a greater SSA, as seen in Figure 4c. That is, ZnO surface coverage occurred earlier on lower SSA supports compared to high SSA supports. The thickness of the loaded ZnO is also reflected in the absorbance. Due to the more dispersed loading of ZnO onto higher SSA supports, their average thickness is smaller, resulting in reduced absorbance as compared to lower SSA supports loaded with ZnO.

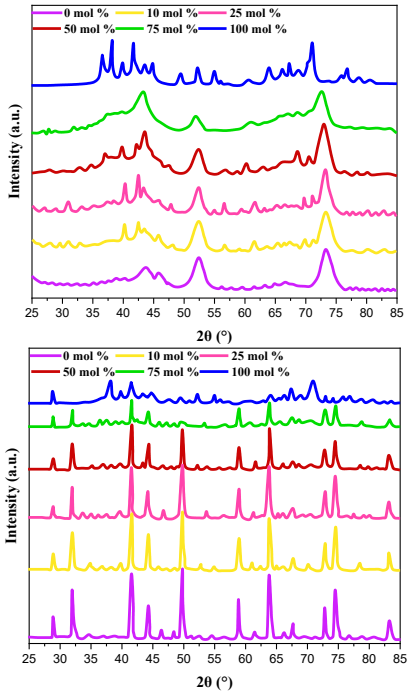

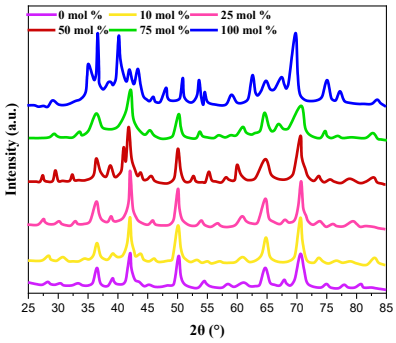

Figure 1. XRD form of A ZnO/γ-TiO_2 (SSA-195), B ZnO/α-TiO_2 (SSA-1.8) and C ZnO/$MgTiO_3$ (SSA-119). The amounts of ZnO loaded are shown by numbers in mol%.

3.2 Reducing Carbon Dioxide with Water via Photocatalysis

Water splitting and CO2 reduction happened concurrently in photocatalytic CO2 reduction with H2O. Fig 5 shows the CO and H2 productivity rates per hour for all samples containing the ZnO placed on the support after 5 hours of reaction. This includes samples with difficult-to-see crystalline phases. Figure 2 shows the result of subtracting the support X-ray diffraction patterns from the observed X-ray patterns. The mined XRD forms showed deflection peaks that may have been α-, γ-, γ-, or ε-phases of zinc oxide, but no peaks that could have been from composite oxides of zinc oxide and aluminum oxide, or zinc oxide and magnesium titanium oxide. Tables 1 and 2 describe the identified ZnO phases, which were achieved by subjecting all samples to the identical procedure. According to the data in the table, the α-phase was the first to appear in most samples as the loaded amount of ZnO increased, followed by the γ- and ε-phases, which both showed increases, and finally the α-phase showed a decrease. The β-phase, which remains stable even at elevated temperatures, appeared and gained prominence as loadings increased. In the unsupported sample of pure ZnO, the β-phase was most prominent, with a little amount of the ε-phase also visible. With the lowest specific surface area (SSA) (1.8 m2/g), the α-phase could not be identified in ZnO/γ-TiO2 (SSA-1.8). At lower loadings, MgTiO3 (SSA-119) did not develop a clear crystalline phase.

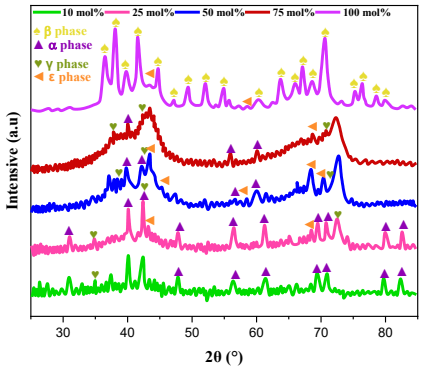

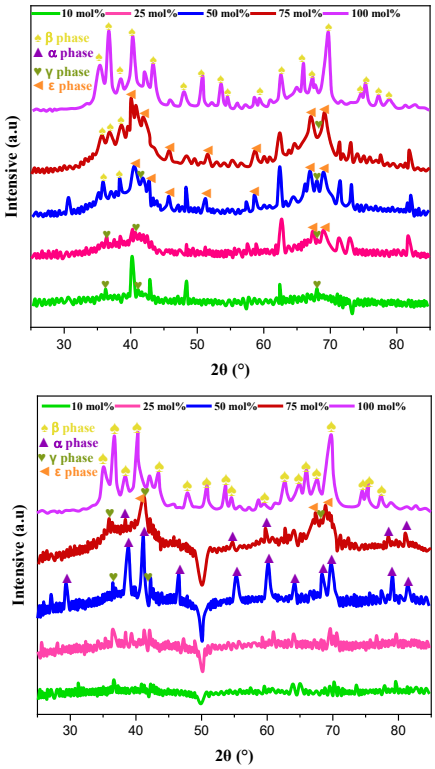

Figure 2. A ZnO/γ-TiO_2 (SSA-195), B ZnO/α-TiO_2 (SSA-1.8), and C ZnO/$MgTiO_3$ (SSA-119) are XRD patterns of ZnO on the support that were obtained by subtracting the XRD from Figure. 1.

Table 2 Outline of ZnO polymorphs

Polymorph	**β-ZnO[6]**	**γ-ZnO[7]**	**α-ZnO[5]**	**ε-ZnO[8]**
Space group	*C2/m*	*Fd−3m*	*R−3c*	*$P6_3mc$*
Structure	Monoclinic	Three-dimensional	Rhombohedral	Hexagonal
Lattice parameter	a = 13.3300 Å b = 4.1400 Å c = 6.9000 Å β = 104.800°	a = 9.3480 Å	a = 4.9825 Å c = 13.4330 Å	a = 2.9036 Å c = 9.2554 Å

The mass disparity between Al and Zn enables the obvious differentiation of rod-shaped ZnO particles from the support. The rods' length dropped from many tens of nanometers to sub-micrometers as the loading quantity of ZnO increased. With the exception of those on α-TiO_2 (SSA1.8), which had a dispersed load and non-contacting particle distribution, a reduced quantity of ZnO loading resulted in particles that were neither dispersed nor touched. The dispersion was more pronounced on supports with a higher SSA.

The X-ray diffraction results presented in Figure 2 c corroborate this observation. The surface morphological change observed on the TiO_2 support was comparable to that of $MgTiO_3$

(surface area-2.6), whose minor surface area prevented the development of mixed oxides. In accordance with the UV–Vis measurements detailed below, these alterations in surface morphology that occurred as the quantity of ZnO loaded increased. Due to the absence of the Al_2O_3characteristic in the electron diffraction pattern, all spots and hallo patterns are regarded as belonging to the crystalline phases of ZnO. This proves that every ZnO on the sustenance was composed of many phases or grains.. Furthermore, the well-crystallized regions suggest that the α and β phases were present, whereas the α- and ε-phases were flawed, as predicted by the pattern. Consistent with the phases identified in the X-ray diffraction patterns, the phases that emerged in the diffraction pattern are identical.

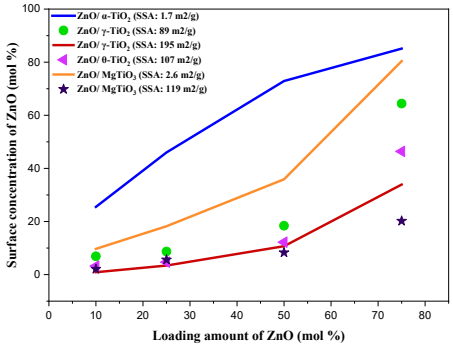

Figure 3 A comparison of the ZnO surface molecular concentrations of all prepared samples, as determined by the Al 2p and Zn 3p XPS peak intensities. The linear correlation between the input quantity for the reference and the surface concentration is depicted by the dotted line.

XPS studies revealed that the peak intensities of Zn 2p and Al 2p fluctuated with the loading amount of ZnO, but there were no noticeable shifts or changes in the widths of these peaks. Support XRD pattern subtraction from sample XRD pattern reveals that ZnO particles were loaded onto the support without TiO_2 mixed oxides or apparent mixing. With respect to ZnO loading, Figure 3 displays the relative strengths of Zn and Al 2p and the consequent atomic concentration ratios. Supports with smaller SSAs allowed the loaded ZnO to cover more surface area more quickly. According to the observation, this is true for ZnO/α-TiO_2 (SSA1.8) and ZnO/$MgTiO_3$ (SSA-2.6).

The three manufactured samples shown in Figure 4 have diffuse reflection UV-V is spectra, which correspond to the samples shown in Figures 2. Since the absorbance of TiO_2 is practically nil in preparation, the absorbance increased as the loading amount of ZnO increased. Hydrogen, carbon monoxide, and oxygen production remained nearly constant after 5 hours of reaction time. The rates of production of hydrogen, carbon monoxide, and oxygen (hereafter abbreviated as [H_2], [CO] and [O_2], respectively) remained in a stoichiometric ratio, meaning that photocatalytic reduction of CO_2 occurred. The Figure clearly shows that the assisted catalyst samples exhibited much better activity for the photocatalytic reduction of CO_2 with water when compared to the 100% ZnO sample. Support has a substantial impact after modifying rates of H_2 and CO production for loaded ZnO mass, as illustrated in Figure 5.

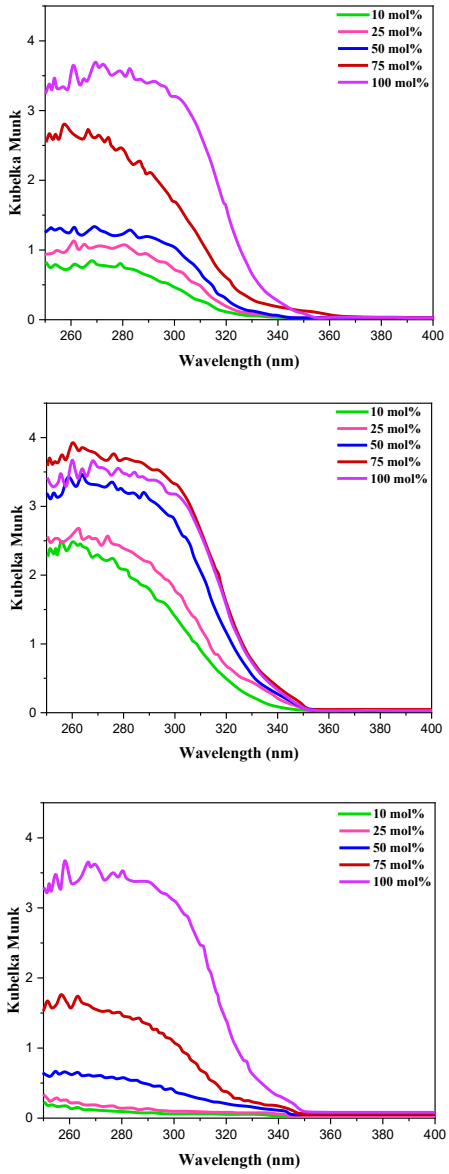

Figure 4. A ZnO/$MgTiO_3$ (SSA-119), B ZnO/γ-TiO_2 (SSA-195), and C ZnO/α-TiO_2 (SSA-1.8) exhibit diffuse reluctance spectra in the UV–Vis. The loaded quantities of ZnO are denoted in mol%.

In relation to the quantity of loaded ZnO, the rates of H_2 and CO production are clearly different. The former increased with decreasing loading and the latter decreased with increasing loading. This points to the possibility of H_2 and CO creation happening separately. Figure 5 shows that normalizing the production rates with the mass of loaded ZnO on the catalysts makes a more quantitative study possible.

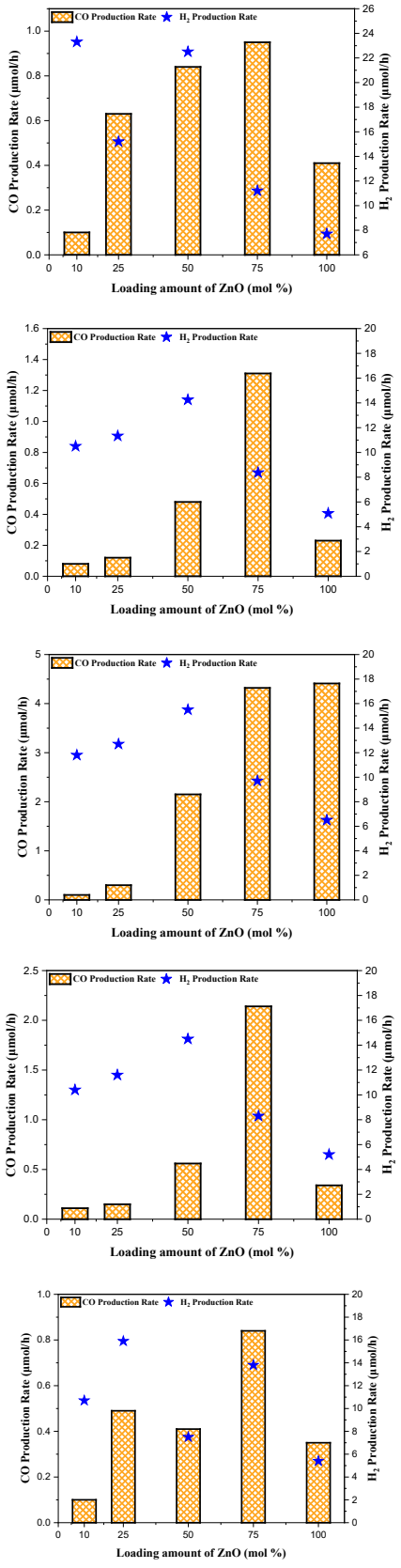

Figure 5. The rates at which H_2 and CO are produced are as follows: A ZnO/γ-TiO_2 (SSA-195), B ZnO/γ-TiO_2 (SSA-89), C ZnO/H-TiO_2 (SSA-107), D ZnO/α-TiO_2 (SSA-1.8), E ZnO/$MgTiO_3$ (SSA-119), and F ZnO/$MgTiO_3$ (SSA-2.6)

3.3 Loaded ZnO Particles Form Crystalline Phases

According to the authors [11], [12], β-ZnO should be produced by calcination (873 K)absenceof a support while the specimen is being prepared. In reality, the β-phase made up the majority of the 100% sample. The ZnO on the support exhibited the α-phase when loaded with a lower amount, but it transitioned to the β-phase as the loaded amount increased. Their lattice constants are noticeably different, even though α-TiO_2 and α-ZnO are both orthorhombic in structure. Their γ-phases likewise exhibit this,because of the gap between the oxygen atoms in TiO_2 is smaller than that in ZnO, compressive stress is exerted on the loaded ZnO. The α-phase of zinc oxide, which is the most stable ZnO phase at high pressure and has the highest density among all the phases, could be observed at lower loading levels of ZnO. The most stable β-phase, the α-phase, was observed at 873 K, when the loading amount was increased. The larger peaks of 30-50 and 60-80° in Figure 2 show that the γ- and ε-phases, which are considered faulty, emerged at the intermediate loading level.Though ZnO is thermodynamically miscible with TiO_2 and $MgTiO_3$[13], [14], [15], XRD and XPS analyses showed that Zn was not dissolved in either TiO_2 or $MgTiO_3$, and ZnO particles were uniformly dispersed across the supports, with just two exceptions.: (1) 24 and 42 mol% ZnO on α-TiO_2 (specific surface area-1.8), and (2) 6 and 12 mol% ZnO on $MgTiO_3$ (SSA-119). The ZnO particles could not withstand being separated initially due to the support having a surface area that was too small (1.8 m2 g−1).

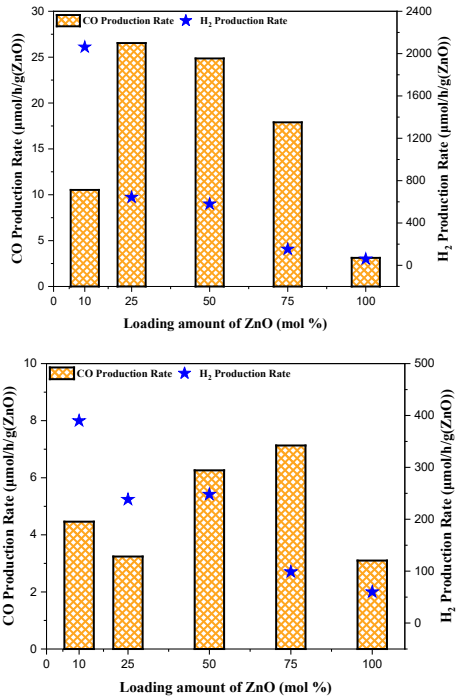

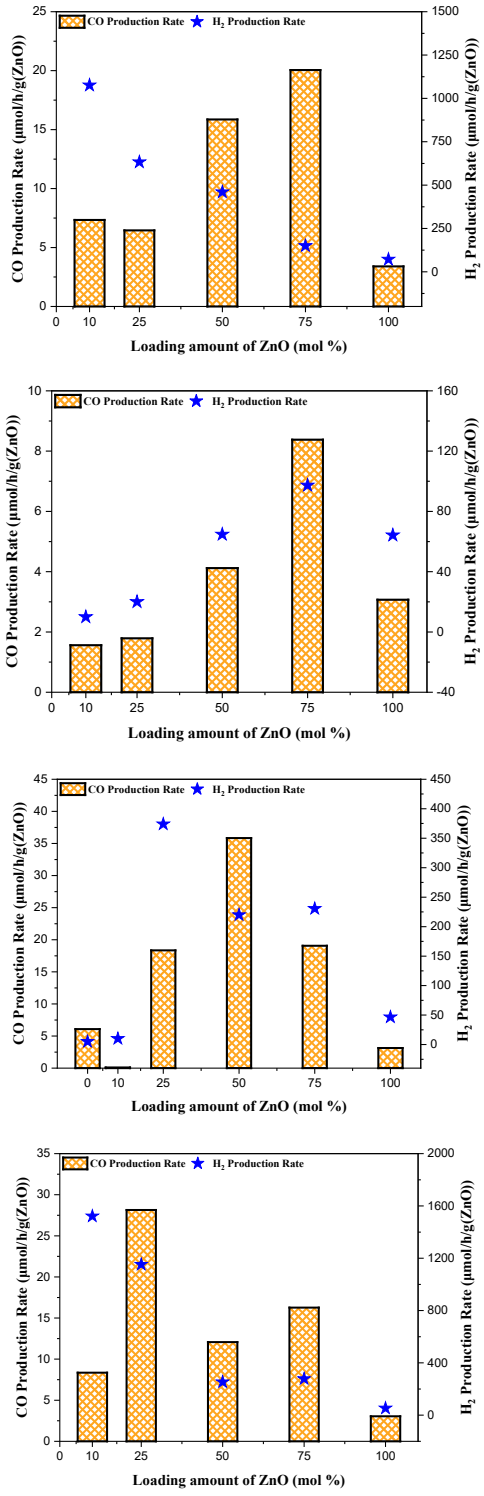

Figure 6. A ZnO/γ-TiO_2 (SSA195), B ZnO/γ-TiO_2 (SSA89), C ZnO/θ-TiO_2 (SSA-107), D ZnO/α-TiO_2 (SSA-1.8), E ZnO/$MgTiO_3$ (SSA-119), and F ZnO/$MgTiO_3$ (SSA-2.6) are the productivity rates of H_2 and CO standardized with the laden ZnO mass.

In Figure 4, the surface concentration of ZnO was evaluated by XPS peak intensities, and the influence of surface area was clearly visible. The regardless of the type of support and the crystalline phases it included, the surface ZnO concentration was substantially greater than the loaded amount of ZnO. The latter situation is most likely brought about by the interaction of the loaded ZnO and $MgTiO_3$. Lower loading amounts are most likely due to ZnO dissolving in $MgTiO_3$. The XRD patterns in Figure 2 shows the insignificance of the mixed oxide concentration. Figures 5 d and e for the two outlier instances that demonstrated weak catalytic activity. It follows that, regardless of Al_2O_3or $MgTiO_3$ and their crystalline phases, ZnO particles should be spread on the support for the photocatalytic activity to be commendable.

3.4 Impact of SSA on Geometry and Catalytic Activities

Our initial step was to determine how the samples' specific surface area (SSA) correlated with their production rates. After 5 hours of photocatalytic CO_2 reduction with water, the four samples with the highest catalytic activity are plotted against SSA to illustrate the rates of H_2 and CO generation. It would appear that both rates are in line with SSA at first estimation. Note that though, that there are four distinct sets of numbers that show the supports' specific surface areas (SSAs), which are far bigger than ZnO's. There is a general trend toward higher ZnO loading amounts for all supports as reaction rates rise. That the support's bigger specific surface area made scattered loading of ZnO possible and that the catalytic activity increased with loading amount until the loaded particles coalesced is in line with the results of the previous section. The next step was to examine how the crystalline phase of the ZnO support affected the rate of H_2 and CO generation.

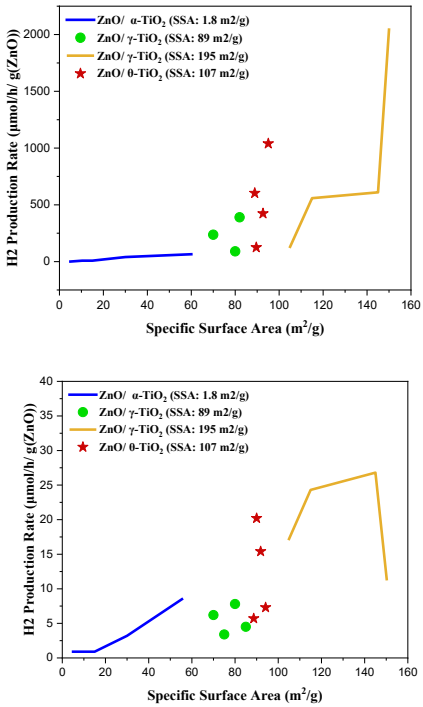

Figure 7. The effects of sample SSA on the rates of hydrogen gas (A) and carbon monoxide (B) production

3.5 Crystalline Phases and Their Impact on ZnO Loading

The crystalline form of zinc oxide may affect its catalytic activity, according to recent research. It has been reported that the addition of mixed phases or the definition of boundaries between different phases can improve photocatalytic activity. According to studies [16], [17], γ- and γ-, α- and γ-, and β-ZnO and GaOOH are some of the ZnO phases that can be combined to enhance activity [18], [19]. Previous research has also shown that mixed phases of γ- and γ-phases on TiO_2 support exhibit significant catalytic activity [20], [21]. The α- and γ-phases are the primary focus of the phase discussion since they had the greatest influence on the catalytic activity in the samples that showed higher levels of activity. Two XRD peaks, 2 = 36.1° for ɨ-ZnO and 2 = 33.8° for ű-ZnO, have been chosen for the purpose of evaluating the relative visibility of the ϱ- and j-phases. The γ/α phase ratio, which is calculated by comparing the peak intensities of the two peaks and their respective peak areas, is illustrated in Fig. 8 a and b, where H_2 and CO generation rates are displayed. For the γ- and α-phases, the abundance ratio is determined by the ratio of these two peaks. It is evident that there is a direct relationship between the rates of H_2 production and the abundance of the α-phase. Meaning, when the α-phase was more abundant, the production of H_2 was higher. The rates of CO generation were not found to be significantly related to the intensity phase ratio. This discovery lends credence to the hypothesis that CO and H_2 production happen independently, as demonstrated before by authors [22], [23], [24].

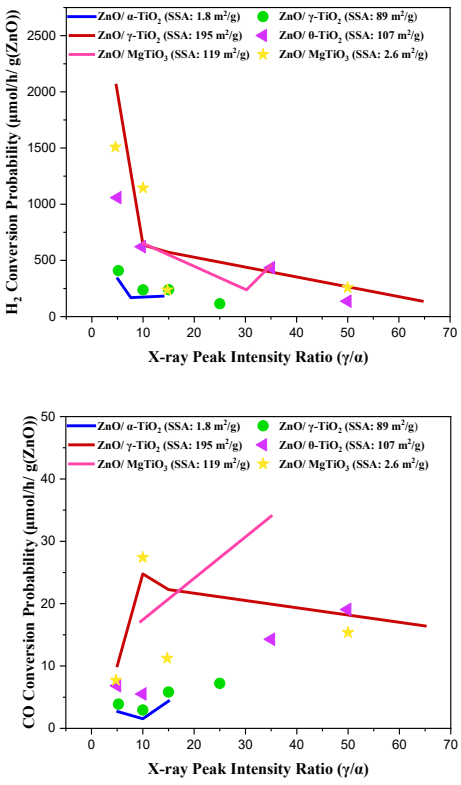

Figure 8. Variations in H_2 and CO production rates, standardized by ZnO mass loaded, as a function of the intensity ratios of X-ray peak (γ/α) for all specimen.

The rates of CO generation for each support either rise with the intensity ratio of X-ray peak or reached their highest point at a certain intensity ratio of X-ray peak, as can be seen more clearly in Figure. 8 b. In addition, samples with a γ/α phase ratio below 15 and increased rates of H_2 formation also present higher rates of CO production. Hydrogen, which is generated when water splits on the α-phase, is thought to have a role in the following CO creation on the γ-phase. Through a photocatalytic process, hydrogen atoms adsorbed on the surface can be created by decreasing the water adsorbing on the α-phase, or H_2O (ad)[25], [26].

$$H_2O(\text{adsorbed}) \rightarrow 2H(\text{adsorbed}) + \frac{1}{2}O \qquad (1)$$

Then, hydrogen atoms adsorbed on the surface moves to the boundariesamong the α-phases and γ-phases to decrease the amount of CO_2 adsorbed on them[27], [28].

$$CO_2(\text{adsorbed}) + 2H(\text{adsorbed}) \rightarrow CO + H_2O \qquad (2)$$

With increased SSA, the γ-phase is recognized to be flawed. Authors [29] state that when CO_2 is adsorbed on ZnO, it assumes the form of monodentate bicarbonate. In order to reduce CO_2 with water in a photocatalytic manner, the monodentate bicarbonate is reduced by hydrogen created during water splitting [30].

To determine the CO generation rate, multiply the H2 production rate by the appropriate conversion factors, assuming that the CO2 reduction follows Reactions (1) and (2) [31], [32], [33].

$$(\text{CO Conversion factor}) \times (\text{production rate of } H_2\ ) = (\text{CO production rate}\ ) \qquad (3)$$

Figure 9 displays the γ/α phase ratio, which is obtained by subtracting the observed H_2 production rates from the measured CO production rates. There is some plot disjointedness, however the technique outlined earlier is shown. When the γ-phase develops, the α-phase decreases, leading to a decrease in the H_2 production rates and an increase in the carbon monoxide productivity rates on the γ-phase. This is because the γ-phase converts CO_2 into CO. Since the γ-phase is increasing and the α-phase is decreasing, the CO generation rate should peak at a specific intensity phase ratio, as seen in Figure 8 b. The two processes can be seen as separate, as proposed in previous studies, due to the fact that the rate of hydrogen generation is significantly higher than the rate of carbon synthesis and only a small portion of hydrogen is utilized for carbon dioxide reduction [34]. The suggested process is not yet refined. To confirm the current method, it would be helpful to do additional investigations employing ZnO mixed phases with α/γ phase ratio adjustment but without support.

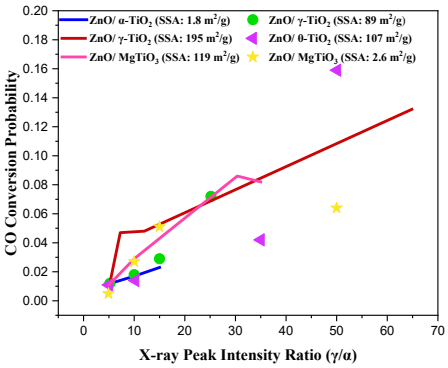

Figure 9. Intensity ratio of X-ray peak (γ/α) is displayed against the conversion factor to CO for all samples.

4. CONCLUSIONS

Studying the crystalline phases and UV light irradiation of ZnO loaded on a support for CO_2 reduction by water was undertaken. The support and loaded material were taken into account during the investigation. Two supports, Al_2O_3 with distinct SSAs and crystal structures and $MgTiO_3$, with a spinel-type crystal structure identical to that of γ-ZnO, were used in the research.

No matter the support, the presence of crystalline phases in ZnO on the surface changed as the loaded ZnO amount increased, except for α-TiO_2 (SSA-1.8). As the loaded quantity increased, the α-phase instead of the β-phase, which is more stable at the current calcination temperature, initially formed. The α-phase is stable at higher pressures. Al-O is capable of compressing ZnO due to the close atomic separation between Al and Zn-O. As soon as the γ-phase became conspicuously differentiated from the β -phase, the γ-phase was formed. As the loading amount increased, the rod-shaped ZnO particles that were spread on the supports showed a slight increase in length from 10-500 nm. Catalytic activity increased as the SSA of the support grew bigger, indicating that the ZnO particles were loaded more dispersedly. The results demonstrate that the activity is highest for ZnO particles put onto the support in the form of rods a few tens of nanometers in diameter.

A lot more activity was visible in the supported samples compared to the non-supported ones. Samples dominated by the α- and α-phase had higher rates of H_2 and CO generation. Nevertheless, their transformation was significantly distinct in relation to the ratio of γ-ZnO to α-ZnO. The rate of H_2 production was directly proportional to the α-phase abundances; that is, more α-phase abundance resulted in more H_2 production. On the other hand, the rate of CO production rose as the γ-ZnO/α-ZnO ratio grew and reached its maximum at a specific γ-ZnO/α-ZnO ratio.

Furthermore, samples exhibiting elevated rates of H_2 generation also exhibit elevated rates of CO production. Based on these findings, we infer that the α-phase or its limits are the primary sites for hydrogen production during water splitting, with the subsequent reduction of CO_2 by the H.

REFERENCES

[1] L. Wang *et al.*, 2023, "Highly Efficient and Selective Visible-light Photocatalytic CO_2 Reduction to CO Using a 2D Co(II)-Imidazole MOF as Cocatalyst and Ru(bpy)3Cl2 as Photosensitizer," *Chem Asian J*, vol. 18, no. 15. DOI:10.1002/asia.202300297

[2] C. Chen, C. Tang, W. Xu, Y. Li, and L. Xu, 2018, "Design of iron atom modified thiophene-linked metalloporphyrin 2D conjugated microporous polymer as CO_2 reduction photocatalyst," *Physical Chemistry Chemical Physics*, vol. 20, no. 14, pp. 9536–9542. DOI:10.1039/C8CP00974K

[3] Roseline, S., Paramasivam, V., Parameswaran, P., Antony, A.G. (2019). Evaluation of mechanical properties and stability of Al 6061 with addition of ZrO2 And Al2O3. Journal of New Materials for Electrochemical Systems, Vol. 22, No. 1, pp. 21-23. DOI:10.14447/jnmes.v22i1.a05

[4] H. Zhao, J. Xu, L. Liu, G. Rao, C. Zhao, and Y. Li, 2016, "CO_2 photoreduction with water vapor by Ti-embedded MgAl layered double hydroxides," *Journal of CO_2 Utilization*, vol. 15, pp. 15–23. DOI:10.1016/j.jcou.2016.04.004

[5] Sankar, L.P., Kamalakannan, R., Aruna, G., Meera, M.R., Vijayan, V., Sivananthan, S. (2020). Mechanical behavior and microstructure evolution of Al-5%Cu/TiC metal matrix composite. Journal of New Materials for Electrochemical Systems, Vol. 23, No. 4, pp. 252-255. DOI:10.14447/jnmes.v23i4.a05

[6] C. Ning *et al.*, 2021 "650 nm-driven syngas evolution from photocatalytic CO_2 reduction over Co-containing ternary layered double hydroxide nanosheets," *Chemical Engineering Journal*, vol. 412. DOI:10.1016/j.cej.2020.128362

[7] N. Yang, Y. Liu, J. Zhu, Z. Wang, and J. Li, 2020, "Study on the efficacy and mechanism of Fe-TiO_2 visible heterogeneous Fenton catalytic degradation of atrazine," *Chemosphere*, vol. 252. DOI:10.1016/j.chemosphere.2020.126333

[8] Sathish, T., Chandramohan, D., Vijayan, V., Sebastian, P.J. (2019). Investigation on microstructural and mechanical properties of Cu reinforced with Sic composites prepared by microwave sintering process. Journal of New Materials for Electrochemical Systems, Vol. 22, No. 1, pp. 5-9. DOI:10.14447/jnmes.v22i1.a02

[9] V. Butera and H. Detz, 2021, "Photochemical CO_2conversion on pristine and Mg-doped gallium nitride (GaN): A comprehensive DFT study based on a cluster model approach," *Mater Chem Front*, vol. 5, no. 23, pp. 8206–8217. DOI:10.1039/D1QM01118Av

[10] C. Wang *et al.*, 2019, "Two-Dimensional Cobaltporphyrin-based Cobalt-Organic Framework as an Efficient Photocatalyst for CO_2 Reduction Reaction: A Computational Study," *ACS Sustain Chem Eng*, vol. 7, no. 16, pp. 14102–14110. DOI:10.1021/acssuschemeng.9b02699

[11] Q. Wang *et al.*, 2021, "Rationally designed plasmonic hybrid coupling structure of Ag/rGO-ZnO for enhanced

photocatalytic CO_2 reduction," *J Alloys Compd*, vol. 887. DOI:10.1016/j.jallcom.2021.161457

[12] Q. Xiao *et al.*, 2024, "Nanostructured ZnO/ZnS with Type-II Hetero-junction for Efficient CO_2 Photoreduction," *Chem Res Chin Univ*. DOI:10.1007/s40242-024-4022-8

[13] L. Liu, 2016, "Controllable ZnO nanorod arrays@carbon fibers composites: Towards advanced CO_2 photocatalytic reduction catalysts," *Ceram Int*, vol. 42, no. 10, pp. 12516–12520. DOI:10.1016/j.ceramint.2016.04.136

[14] I. M. Hegazy, R. A. Geioushy, S. M. El-Sheikh, A. Shawky, S. El-Sherbiny, and A.-H. T. Kandil, 2020, "Influence of oxygen vacancies on the performance of ZnO nanoparticles towards CO_2 photoreduction in different aqueous solutions," *J Environ Chem Eng*, vol. 8, no. 4. DOI:10.1016/j.jece.2020.103887

[15] Q. Wang *et al.*, 2022, "An in situ-fabricated p-Co3O4@n-ZnO surface heterojunction photocatalyst for solar-to-fuel conversion of CO_2," *Mater Chem Front*, vol. 7, no. 3, pp. 523–534. DOI:10.1039/D2QM00850E

[16] K. Shanmuganandam, S. Thanikaikarasan, T. Ahamad, S. Ali, and V. P. Sundramurthy, 2022, "Structure, Surface Nature, Thermal Stability, and Biomass Gasification Process of NiO/SiO2and NiO-Pr2O3/SiO2Nanocomposites Obtained through Facile Deposition Precipitation Method," *J Nanomater*, vol. 2022. DOI:10.1155/2022/1479808

[17] R. H. Al-Serwi *et al.*, 2022, "Molecular Docking and Green Synthesis of Bioinorganic TiO_2Nanoparticles against E.coli and S.aureus," *Bioinorg Chem Appl*, vol. 2022. DOI:10.1155/2022/1142727

[18] M. K. Sharma *et al.*, 2023, "Cellulose fortified bio-composite film preparation using starch isolated from waste avocado seed: starch properties and film performance," *Biomass Convers Biorefin*. DOI:10.1007/s13399-023-05058-z

[19] B. Tessema, G. Gonfa, S. M. Hailegiorgis, S. V Prabhu, and S. Manivannan, 2023, "Synthesis and characterization of silver nanoparticles using reducing agents of bitter leaf (Vernonia amygdalina) extract and tri-sodium citrate," *Nano-Structures and Nano-Objects*, vol. 35. DOI:10.1016/j.nanoso.2023.100983

[20] K. Sahile, S. V Prabhu, and A. Worku, 2023, "Development of Enhanced Ultraviolet Resistance Hybrid Cotton Fabric using Functionalized Biocarbon derived from Teff (Eragrostis tef) Hay," *Asian Journal of Chemistry*, vol. 35, no. 6, pp. 1477–1484. DOI:10.14233/ajchem.2023.27898

[21] D. Dinesh Kumar *et al.*, 2023, "Study of Microstructure and Wear Resistance of AA5052/B4C Nanocomposites as a Function of Volume Fraction Reinforcement to Particle Size Ratio by ANN," *J Chem*, vol. 2023. DOI:10.1155/2023/2554098

[22] W. Alghamdi, S. Mayakannan, G. A. Sivasankar, J. Singh, B. Ravi Naik, and C. Venkata Krishna Reddy, 2023, "Turbulence Modeling Through Deep Learning: An In-Depth Study of Wasserstein GANs," in *Proceedings of the 4th International Conference on Smart Electronics and Communication, ICOSEC 2023*, Institute of Electrical and Electronics Engineers Inc., pp. 793–797. DOI:10.1109/ICOSEC58147.2023.10275878

[23] A. M. Gejea, S. Mayakannan, R. M. Palacios, A. A. Hamad, B. Sundaram, and W. Alghamdi, 2023, "A Novel Approach to Grover's Quantum Algorithm Simulation: Cloud-Based Parallel Computing Enhancements," in *Proceedings of the 4th International Conference on Smart Electronics and Communication, ICOSEC 2023*, Institute of Electrical and Electronics Engineers Inc., pp. 1740–1745. DOI:10.1109/ICOSEC58147.2023.10276383

[24] R. Girimurugan, C. Shilaja, A. Ranjithkumar, R. Karthikeyan, and S. Mayakannan, 2023 "Numerical Analysis of Exhaust Gases Characteristics in Three-Way Catalytic Convertor Using CFD," in *AIP Conference Proceedings*, B. A. Sunil J., Ed., American Institute of Physics Inc. DOI:10.1063/5.0150561

[25] M. Mgolombane, S. Majodina, O. M. Bankole, E. E. Ferg, and A. S. Ogunlaja, 2021, "Influence of surface modification of zinc oxide–based nanomaterials on the photocatalytic reduction of carbon dioxide," *Mater Today Chem*, vol. 20. DOI:10.1016/j.mtchem.2021.100446

[26] H. He, S. Sekoulopoulos, and S. Zygmunt, 2016, "Single-electron activation of CO_2 on graphene-supported ZnO nanoclusters: Effects of doping in the support," *Journal of Physical Chemistry C*, vol. 120, no. 30, pp. 16732–16740. DOI:10.1021/acs.jpcc.6b04526

[27] C. Shi, L. Zhang, Z. Shi, J. Ma, and Z. Wang, 2022, "Cellulose template designed porous ZnO based catalysts with different valence copper for solar photocatalytic CO_2 conversion," *Ind Crops Prod*, vol. 186. DOI:10.1016/j.indcrop.2022.115223

[28] J. M. L. Gaol and T. Imae, 2023 "CuO/ZnO catalysts in chitosan film for CO_2 reduction," *J Environ Chem Eng*, vol. 11, no. 6. DOI:10.1016/j.jece.2023.111333

[29] S. Liu, J. Wang, and J. Yu, 2016, "ZIF-8 derived bimodal carbon modified ZnO photocatalysts with enhanced photocatalytic CO_2 reduction performance," *RSC Adv*, vol. 6, no. 65, pp. 59998–60006. DOI:10.1039/C6RA11264A

[30] V. Balan, S. Ramakrishnan, G. Palani, And M. Selvaraju, 2024 "Investigation on The Enhancement Of Heat Transferin Counterflow Double-Pipe Heat Exchangerusing Nanofluids," *Thermal Science*, vol. 28, no. 1A, pp. 233–240. DOI:10.2298/TSCI230312273V

[31] Q. Liu, M. Xu, B. Zhou, R. Liu, F. Tao, and G. Mao, 2017, "Unique Zinc Germanium Oxynitride Hyperbranched Nanostructures with Enhanced Visible-Light Photocatalytic Activity for CO_2 Reduction," *Eur J Inorg Chem*, vol. 2017, no. 15, pp. 2195–2200. DOI:10.1016/j.jcis.2022.08.048

[32] X. Ma *et al.*, 2022, "Fiber-like ZnO with highly dispersed Pt nanoparticles for enhanced photocatalytic CO_2 reduction," *J Colloid Interface Sci*, vol. 628, pp. 768–776. DOI:10.1016/j.jcis.2022.08.048

[33] J. Zhao *et al.*, 2022, "In situ construction of 1D/2D ZnO/graphdiyne oxide heterostructures for enhanced photocatalytic reduction in a gas phase," *Mater Chem Front*, vol. 6, no. 21, pp. 3205–3212. DOI:10.1039/D2QM00349J

[34] Ó. R. Andrade, V. Rodríguez, R. Camarillo, F. Martínez, C. Jiménez, and J. Rincón, 2022, "Photocatalytic Reduction of CO_2 with N-Doped TiO_2-Based Photocatalysts Obtained in One-Pot Supercritical Synthesis," *Nanomaterials*, vol. 12, no. 11. DOI:10.3390/nano12111793

[35] S.Dinesh, A.Godwin Antony, S.Karuppusamy, V.Vijayan and B.Suresh Kumar, 2016. Experimental investigation and optimization of machining parameters in CNC turning operation of duplex stainless steel. Asian Journal of Research in Social Sciences and Humanities 6,pp. 179-195. DOI:10.5958/2249-7315.2016.01006.6

[36] S.Dinesh, A.Godwin Antony, K.Rajaguru and V.Vijayan. 2016. Experimental investigation and optimization of material removal rate and surface roughness in CNC turning of EN24 alloy steel, Mechanics and Mechanical Engineering, 20 (4) 451—466. DOI:10.5958/2249-7315.2016.00654.7

[37] T.Tamizharasan, N.Senthil Kumar, V. DOI:10.1007/s42452-019-0170-8, S.Dinesh, 2019. Taguchi's Methodology of optimizing turning parameters over chip thickness ratio in machining PM AMMC, SN Appl. Sci. 1: 160., Springer Publishers. DOI:10.1007/s42452-019-0170-8